Universal progression of structure and dynamics in colloidal nanocrystal gels during salt-accelerated aging

Charles K. Ofosu,[1] Diana L. Conrad,[1,†] William D. Brackett,[3,†] Dingwen Qian,[3] Tsung-Lun Lee,[3] Jiho Kang,[3] Jinny Choi,[1] Anna Bessmertnaya,[1] Jessica D. Oberlander,[1] Allison M. Green,[3] Felix Lehmkhler,[4,5] Andrei Fluerasu,[6] Eric V. Anslyn[1,*] Thomas M. Truskett[2,3,*] Delia J. Milliron[1,2,3*]

[1]Department of Chemistry, University of Texas at Austin, 2506 Speedway, Austin, Texas 78712, USA
[2]Department of Chemical Engineering, University of Michigan, Ann Arbor, MI 48109, USA
[3]McKetta Department of Chemical Engineering, University of Texas at Austin, 200 E Dean Keeton St, Austin, Texas 78712, USA
[4]Deutsches Elektronen-Synchrotron DESY, Notkestr. 85, 22607 Hamburg, Germany
[5]The Hamburg Centre for Ultrafast Imaging, Luruper Chaussee 149, 22761 Hamburg, Germany
[6]National Synchrotron Light Source II, Brookhaven National Laboratory, Upton, NY 11973-5000, USA

† These authors contributed equally.

***Corresponding authors:** anslyn@austin.utexas.edu (E.V.A.); truskett@umich.edu (T.M.T.); milliron@umich.edu (D.J.M.)

Controlling the structure and function of colloidal gels requires a detailed understanding of how the various components govern network formation and aging. In particular, molecular additives like salts are widely used to tune interparticle interactions, yet their influence on gelation pathways in complex systems such as colloidal nanocrystal gels remains inadequately understood. Here, we investigate how non-coordinating salts modulate the evolution of gels formed using chemically-linked tin-doped indium oxide nanocrystals. Through combined structural, dynamic, and kinetic analyses, we demonstrate that increasing salt concentration accelerates gelation. When rescaled by salt-dependent characteristic times, the evolution collapses onto universal trajectories, revealing a time-salt superposition principle. The universality extends across length scales suggesting a single salt-dependent mechanism that controls both local structuring and macroscopic network formation. This observed salt modulation of structure and dynam-

ics provides a predictive basis for controlling the kinetics of non-equilibrium nanocrystal gel assembly, enhancing the rational design of functional nanomaterials with tunable properties.

INTRODUCTION

Due to the resonant interaction of their free charge carriers with light, plasmonic colloidal semiconductor nanocrystals (NCs) have emerged as versatile building blocks for optically active assemblies (*1, 2*). While their individual properties are size- and composition-dependent, assemblies of NCs can exhibit emergent, structure-dependent behaviors, such as coupling of their localized surface plasmon resonances (LSPRs). The opportunity for tailoring optical responses has motivated extensive research into post-synthetic assembly techniques (*3–9*). One promising approach is gelation, whereby NCs form space-spanning percolated networks that exhibit solid-like mechanical properties. These NC gels offer precise and reproducible structural control, making them highly attractive as tunable and responsive optical materials (*10*). Despite advances in assembly techniques, NC gels are fundamentally out-of-equilibrium systems, raising open questions about their formation and evolution (*11–13*). As kinetically arrested materials, they age through local and cooperative rearrangements driven by thermal fluctuations and residual stresses (*14, 15*), resulting in a slow evolution of viscoelastic properties across broad time and length scales. This physical aging is strongly influenced by sample history and preparation protocols (*16*).

Recent studies of tin-doped indium oxide (ITO) NCs cross-linked via dynamic covalent hydrazone bonds show that the structural evolution of the gels is modulated by salt concentration (*17*). In particular, the structure factor, obtained via small-angle X-ray scattering (SAXS), after a given waiting time, evolves systematically with the amount of tetrabutylammonium hexafluorophosphate ($TBAPF_6$) added to the gelation solution. Increases in the primary peak magnitude and deepening of the correlation well suggest a salt-dependent coarsening behavior consistent with structural evolution toward arrest (*18*). The structural evolution and optical modeling of the gels supports a correspondence between salt addition and structural aging in

time. A time–salt superposition relationship, reminiscent of phenomena observed in other spontaneously aging soft matter systems where salt modulates structural evolution (*19–22*), is thus hypothesized to describe the evolution of these colloidal NC assemblies.

However, comprehensive studies addressing how salt impacts the microscopic dynamics and structure of colloidal NC gels remain limited. This gap arises from several challenges. First, early-stage cluster formation occurs at the nanometer scalea length scale challenging to probe using conventional approaches such as rheology or optical microscopy. Second, the multicomponent nature of NC dispersions gives rise to complex fluid behavior, characterized by multiple interaction types and length scales that generate micro- to mesoscale structural heterogeneity, making the interpretation of experimental data nontrivial (*23–26*). Third, most macroscopic probes cannot resolve non-ergodic behavior, where the time-averaged dynamics of a given NC or structural domain deviate from the ensemble average (*27*), thereby requiring experimental data to be both ensemble-averaged and sufficiently time-resolved to capture the detailed evolution of structure and dynamics (*28*). Yet, a detailed understanding of how salt influences the microscopic mechanisms governing structure and dynamics during colloidal NC gelation is essential both from a fundamental physics perspective and for the rational design of functional gel-based nanomaterials.

Herein, we ask: *How does salt addition influence gelation and aging in chemically linked colloidal NC gels?* To address this question, we systematically trace the entire gelation pathway *in situ*from stable dispersion through to aged gelat varying salt concentrations. By leveraging hydrazone chemistry as a linking scheme, we establish a controlled model NC gel system and monitor its evolution over broad time and length scales using SAXS, optical absorption spectroscopy, and X-ray photon correlation spectroscopy (XPCS), the latter of which probes NC dynamics within evolving fractal networks.

We find that salt addition accelerates network formation and modulates the timescales of structural and dynamic evolution, yet the final steady-state structure remains salt-independent. When rescaled by salt-specific characteristic times, structural and dynamic data across salt con-

centrations collapse onto master curves, thus indicating a time–salt superposition phenomenon, and revealing a universal kinetic pathway of gelation. Further analysis of the dynamic data reveals that this universality spans the accessible length scales, indicating a single salt-dependent mechanism that governs both local structuring and macroscopic network formation. Measurements of the effective pairwise interactions without chemical linking, and simulations of the gelation kinetics, identify electrostatic screening as a key driver of faster gelation. Furthermore, kinetic NMR analyses of the chemical bonding underpinning network formation also confirm that reaction rates increase with salt concentration. Altogether, this work demonstrates that additives like salt modulate gelation through molecular- and nanoscale mechanisms, providing guidelines in fabricating colloidal networks with targeted structural and dynamic properties.

RESULTS

Preparation of NC Building Blocks and Gelation

Linker-mediated NC gels were fabricated by first synthesizing oleate-capped indium tin oxide (OL-ITO) NCs using a modified slow-injection method (*29*), yielding stable and uniform NCs with a narrow size distribution. Bright-field scanning transmission electron microscopy (STEM, Fig. 1b) and SAXS analysis (Fig. 1d) analyses confirmed their spherical morphology and low size dispersity. The NC form factor $P(q)$, obtained from SAXS measurements with the scattering wavevector $|q| = 4\pi \sin(\theta/2)/\lambda$ (where θ is the scattering angle and λ the X-ray wavelength), was accurately captured by an analytical spherical model with a core diameter of $\sigma_{\text{core}} = 15.9$ nm and a narrow size distribution (9% standard deviation). The tin doping concentration was 5.2 at%. To prepare the NCs for gelation experiments, the oleate ligands on the ITO NCs were replaced via direct ligand exchange with aldehyde-terminated ligands (AL) (Fig. 1a), which were synthesized using established protocols (fig. S1) (*8*). These ligands contain an aldehyde terminal group for linking, a polyethylene glycol (PEG)-like solubilizing backbone, and a tri-carboxylate anchoring group for binding to the NC surface. Dispersions of AL-capped ITO NCs (AL-ITO) in *N,N*-Dimethylformamide (DMF) were prepared at vari-

ous $TBAPF_6$ concentrations ranging from $0 - 100$ mM. Gelation was initiated by introducing a bifunctional molecular linker with four PEG repeat units, hydrazide $-$ PEG_4 $-$ hydrazide, at a fixed linker-to-colloid ratio, Γ ($\Gamma = 200$), to the AL-ITO dispersions containing varying salt concentrations. This linker promotes dynamic covalent bonding via hydrazone formation between the aldehyde end groups on the ligands and the hydrazide groups on the linker, driving a time-dependent transformation from a free-flowing dispersion to a viscoelastic gel. Scanning electron microscopy of dried gels revealed a network of interconnected NCs (Fig. 1c). The structure factor $S(q)$, which characterizes the mesoscale organization of the NCs, was extracted from the total X-ray scattering cross section using the form factor obtained from dilute OL-ITO dispersions in toluene at a NC core volume fraction $\Phi = 0.0005$. Notably, $S(q)$ profiles of gels aged for 12 months were indistinguishable across all $TBAPF_6$ concentrations (Fig. 1e), indicating that the final structure of the gel is independent of the initial salt concentration.

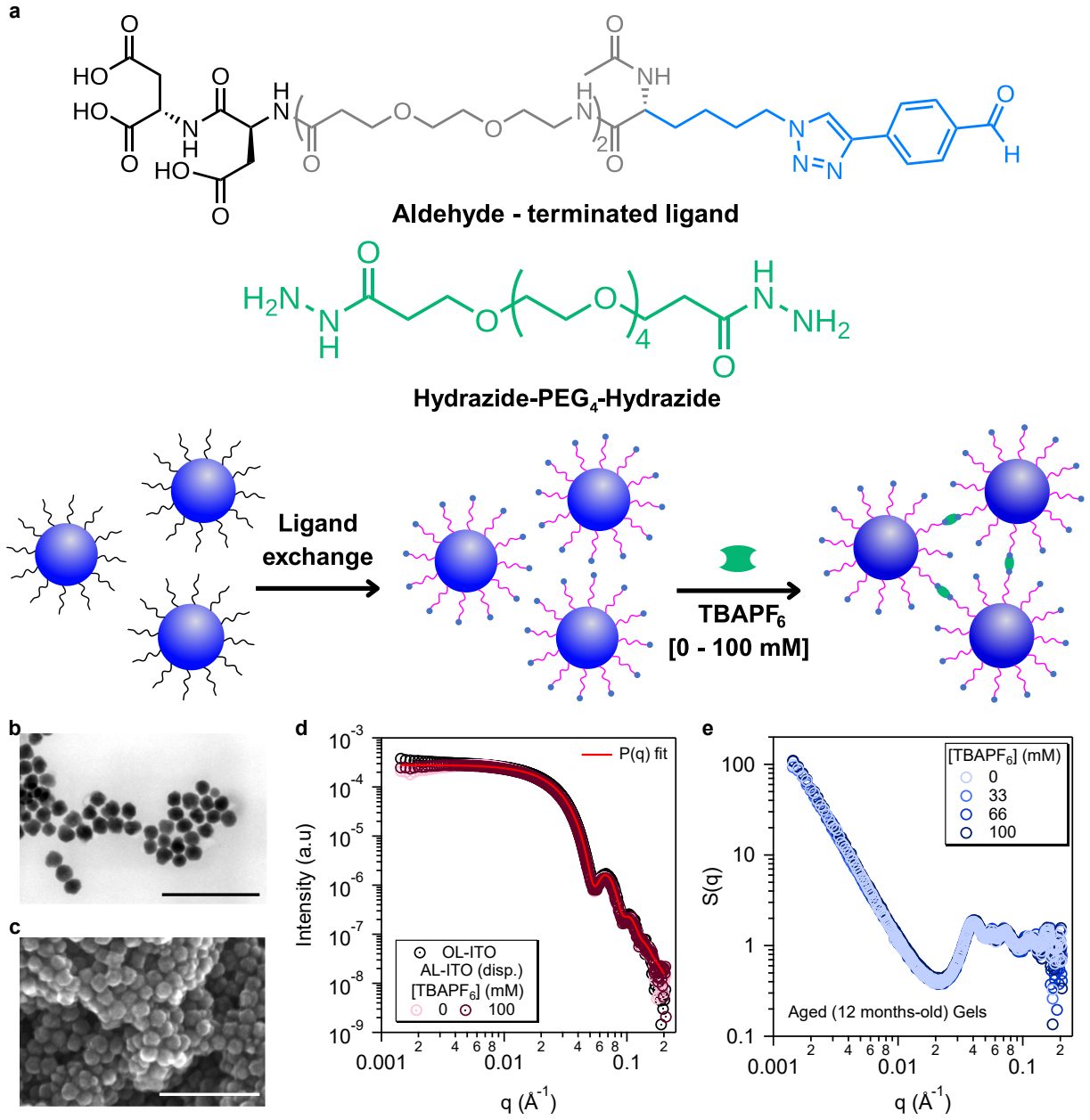

Fig. 1: Preparation of AL-ITO NCs and Gels. **(a)** Schematic illustration of the ligand-exchange process, where oleate-capped ITO (OL-ITO) NCs are functionalized with aldehyde-terminated ligands (AL) to form AL-ITO. The AL-ITO NCs are then linked via the chemical linker hydrazide-PEG_4-hydrazide to form the gel network. STEM image of the ITO NCs **(b)** before ligand exchange (OL-ITO), and SEM **(c)** after ligand exchange (AL-ITO) and linker addition, showing gel network formation (Scale bars = 100 nm). **(d)** SAXS form factors $P(q)$ of dilute (core volume fraction $\Phi = 0.0005$) OL-ITO in toluene and AL-ITO samples in DMF at 0 mM and 100 mM $TBAPF_6$ concentrations. Spherical model form factor fits $P(q)$ (red curve) to the data confirm the spherical morphology, the uniform size (core diameter $\sigma_{\text{core}} = 15.9$ nm) and the small size dispersity (9%) of the NCs. **(e)** Structure factors $S(q)$ of the aged (12-months old) gels made from AL-ITO dispersions at a inorganic core volume fraction $\Phi = 0.03$ prepared at $TBAPF_6$ concentrations of 0, 33, 66, and 100 mM.

Evolution of Microstructure

Following the addition of the molecular linker to AL-ITO dispersions at NC core volume fraction $\Phi = 0.03$, SAXS measurements were performed for a series of salt concentrations at various wait times t_w throughout the gelation process, with t_w defined as the time elapsed after linker addition. Structural evolution was characterized via $S(q)$ analyses (Fig. 2a and fig. S2). Consistent with previous studies (*17, 30*), the temporal evolution of $S(q)$ as a function of q shows a growing signal intensity at the lowest accessible q over time. This increase indicates the development of long length-scale density fluctuations, corresponding to the formation of inhomogeneities associated with network formation or spinodal phase separation. Experimentally, the AL-ITO and linker mixture undergoes visible phase separation over time, evidenced by the emergence of a clear, nanocrystal-poor supernatant in the capillaries containing the aged gels. To systematically compare the effects of salt concentration on the gelation mechanism at structurally equivalent states, it is important to define a system-dependent time corresponding to a point at which the system reaches a common structural state during its evolution. Because macroscopic phase separation can lag behind microscopically detectable changes, we estimate this time point based on the low-q behavior of $S(q)$. Specifically, we extrapolated $S(q)$ to $q \to 0$ by fitting the low-q region of the scattering profile to the OrnsteinZernike form (*31*) (fig. S3):

$$S(q) \approx \frac{S(0)}{1 + (q\xi)^2}, \tag{1}$$

where ξ is the thermal correlation length representing the spatial scale over which density fluctuations are correlated. Conditions where phase separation occurs can be approximately located by the condition $S(0) \geq 10$ (*32, 33*). Therefore, we use the time, t_{10}, at which $S(0) \approx 10$ as a threshold marking the onset of large-scale structure formation consistent with spinodal decomposition. Using this threshold, we define a dimensionless time scale, t_w/t_{10}, which facilitates direct comparison of gel evolution across salt concentrations. Characteristic times marking the onset of structural changes during gelation have similarly been identified based on thresholds monitored by rheology (*34*), SAXS (*20, 35*), or other techniques in previous studies.

We find that t_{10} decreases approximately linearly with increasing salt concentration (Fig. 2b),

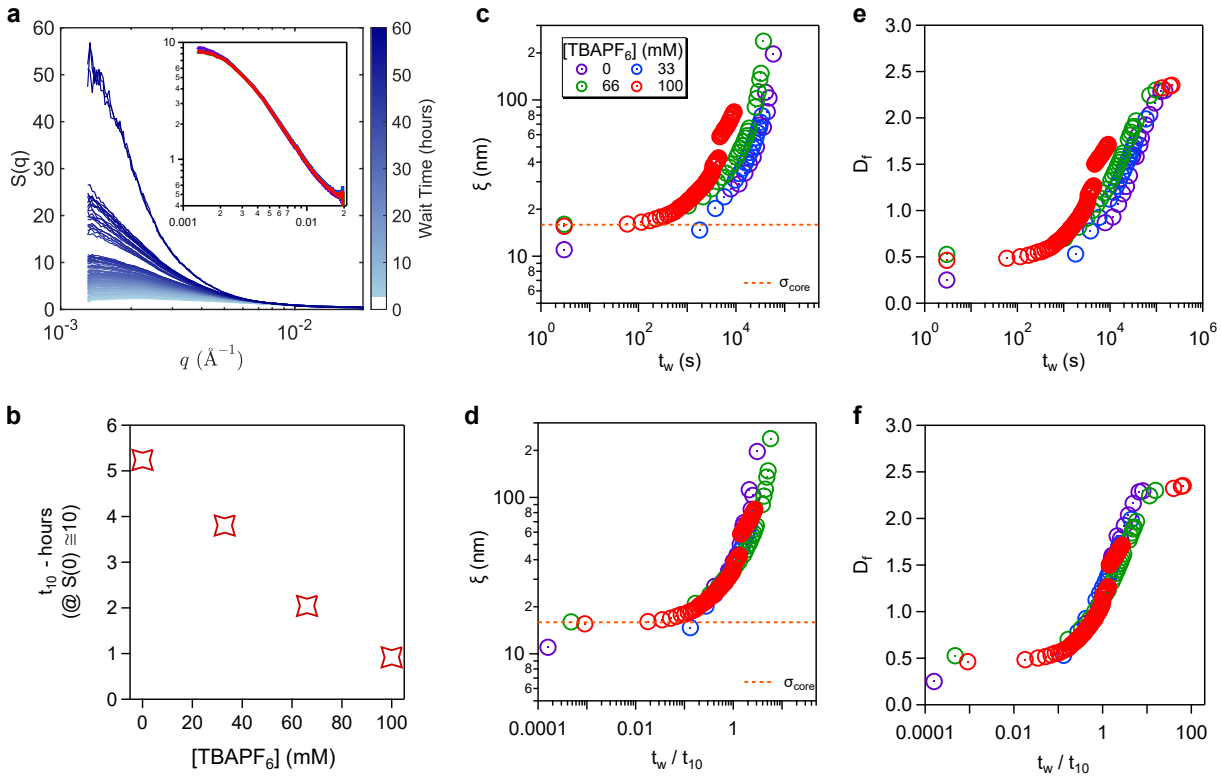

Fig. 2: Microstructure evolution observed via SAXS. (a) $S(q)$ evolution of AL-ITO NCs containing 100 mM $TBAPF_6$ after linker addition at a constant linker-to-NC ratio ($\Gamma = 200$) over a 60-hour gelation period. Inset shows the $S(q)$ at the characteristic time point for the various $TBAPF_6$ concentrations, defined as the time where $S(0) \simeq 10$. **(b)** Characteristic transition time t_{10}, defined according to inset of **a**, as a function of $TBAPF_6$ concentration. Correlation length (ξ) and mass fractal dimension (D_f) of the heterogeneous domains formed during network formation at varying salt concentrations **(c** and **e)** over wait time (t_w) and **(d** and **f)** over normalized wait time (t_w/t_{10}) showing universal progression of microstructure.

demonstrating that salt accelerates the gelation rate. Moreover, the $S(q)$ at t_{10} across different salt concentrations collapse onto a single curve (inset, Fig. 2a), indicating that the mesoscale structure of the gel at this point is independent of the amount of salt added. Correspondingly, ξ, which physically describes the typical size of clusters or correlated domains within the gel network, increases with wait time, reaching larger values more quickly for higher salt concentrations. For all salt concentrations investigated, the increase in ξ is exponential with time, consistent with reaction-limited cluster aggregation (RLCA) kinetics (*36*), where the linking rate governs the aggregation and network formation. The power law behavior of a diverging $S(q)$ at low q is consistent with a fractal network structure (*8, 17*), with $I(q) \sim S(q) \propto q^{-D_f}$

fits yielding the mass fractal dimension (D_f) values (Figs 2e-f). Like ξ, the rate of increase in D_f increases with added salt, before eventually plateauing at $D_f \approx 2.2$ at long wait timesa value typical of colloidal gels and RLCA aggregates (Fig. 2c-d) (*9,17,36,37*). When normalized by their respective t_{10} values, the time dependencies of both ξ and D_f collapse across all salt concentrations over the full temporal evolution of the gels, revealing a timesalt superposition consistent with a universal progression of microstructure. This universality of the structural evolution holds regardless of the value of $S(0)$ used to specify the characteristic time, confirming the robustness of the observation (figs. S4–5).

Structural evolution of the NC gel networks also produces temporal optical modulation of plasmonic optical spectra (*17, 37*). The redshift in the absorption peak is a manifestation of enhanced LSPR-LSPR coupling as NCs become nearer to each other (Fig. 3a, fig. S6) (*6, 8, 9, 17, 38, 39*). Like the structural parameters from SAXS, we find that the time-dependent optical extinction spectra of the gels also depend on the salt concentration (*17*). Specifically, the absorbance spectra and LSPR peak positions progressively broaden and redshift, respectively, upon linker addition (Fig. 3a, c and fig. S6). The half point ($t_{0.5}$) of the LSPR peak position versus time relationship, obtained from a sigmoidal fit (fig. S7), decreases approximately linearly with salt concentration (Fig. 3b). At all salt concentrations, the full width at half maximum (FWHM) increases with wait time, a consequence of the inhomogeneous broadening of the LSPR peak, reflecting microstructural heterogeneities that emerge during network formation (Fig. 3e, fig. S8) (*39, 40*). The rate of increase of the FWHM, for a given wait time, increases with salt concentration (fig. S8), consistent with salt-induced acceleration of gelation. Like in the SAXS analyses, an approximate time–salt superposition of structure-dependent optical response parameters is obtained when the t_w is normalized by $t_{0.5}$ (Fig. 3d, f, fig. S7−8), reinforcing the universal structure transformation that occurs in these linked NC networks.

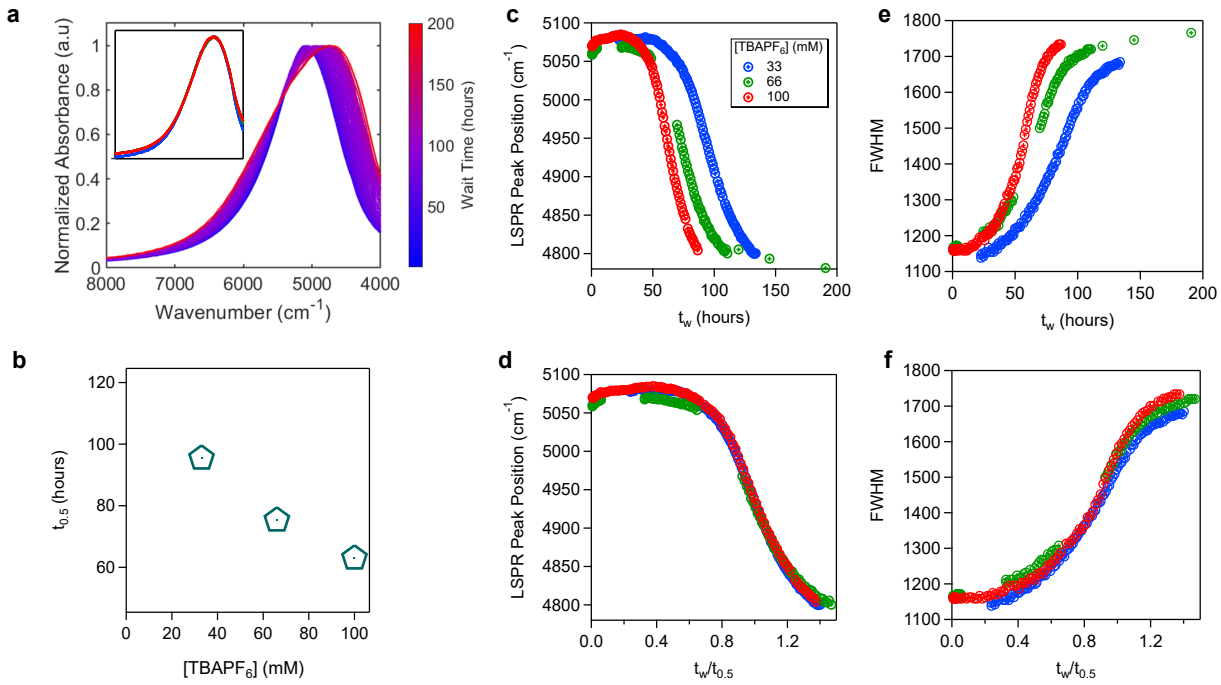

Fig. 3: Microstructure evolution observed via optical spectroscopy. **(a)** Normalized absorbance spectra recorded over time ($0-270$ hours) for an evolving NC gel ($\Phi = 0.002$) containing 100 mM $TBAPF_6$ and $\Gamma = 200$, showing a red shift in the spectra during gelation. Inset shows the normalized absorption spectra at the respective half-point of the LSPR peak position vs wait time t_w function at the point for the various $TBAPF_6$ concentrations. For the optical studies, Φ was reduced by an order of magnitude relative to the SAXS studies to maintain absorbance within detectable limits, which likely contributes to the slower time evolution of the gels. **(b)** Half-point ($t_{0.5}$) of the progression of the LSPR peak position as a function of salt concentration, illustrating the role of the salt in accelerating the gelation process. The result for $t_{0.5}$ at $[TBAPF_6] = 0$ mM is not shown, as the gelation kinetics were too slow for gelation signatures to be observed optically. **(c)** LSPR peak positions extracted from absorbance spectra at different salt concentrations as a function of waiting time, t_w, with **(d)** showing the half-point normalized relationship. **(e)** Temporal evolution of the full width at half maximum (FWHM) of the LSPR at varying salt concentration, with **(f)** showing the half-point normalized relationship. Both the LSPR peak position and FWHM, when plotted as a function of normalized time, corroborate the universal structural evolution during gelation.

Evolution of Microscopic Dynamics

The microscopic dynamics of the dispersion-to-gel transition were probed using X-ray photon correlation spectroscopy (XPCS). XPCS, an X-ray analog of dynamic light scattering (DLS), analyzes temporal correlations in the scattered X-ray intensity to extract dynamic information in real time on microsecond scales (*41–44*). Unlike DLS, XPCS can resolve dynamic processes in non-ergodic systems across nano- to micron-scales, which is critical for obtaining a deeper understanding of colloidal nanoparticle gelation (*34, 45*). The intensity autocorrelation function of XPCS is defined as:

$$g_2(q, \Delta t) = \frac{\langle I(q,t) I(q, t+\Delta t) \rangle}{\langle I(q,t) \rangle^2}, \tag{2}$$

where $I(q,t)$ is the scattered intensity at wave vector q and time t. Angle brackets denote ensemble averaging over all equivalent times t and detector pixels. The accessible lag times Δt are determined by the detector frame rate and total acquisition duration. The intensity correlation function is related to the intermediate scattering function $g_1(q, \Delta t)$ through the Siegert relation:

$$g_2(q, \Delta t) = 1 + b|g_1(q, \Delta t)|^2, \tag{3}$$

where b is the speckle contrast, determined by factors such as the beam coherence, detector pixel and beam size, and measured independently using a porous ceramic membrane as a static reference sample.

The intermediate scattering function $g_1(q, \Delta t)$ characterizes the systems dynamics. After correcting for the baseline and coherence factor post-measurement (fig. S9), we obtain $|g_1(q, \Delta t)|^2$ (Fig. 4), which is then modeled using a Kohlrausch-Williams-Watts (KWW) function of the form (*46–48*):

$$g_1(q, \Delta t) = [1 - f(q)] \exp\left[-\left(\frac{\Delta t}{\tau(q)} \right)^{\beta(q)} \right] + f(q), \tag{4}$$

where $\tau(q)$ is the characteristic relaxation time, $\beta(q)$ is the KWW exponent that reflects the distribution of relaxation times, and $f(q)$ is the non-ergodicity parameter, representing the plateau value of $g_1(q, \Delta t)$. The robustness of the KWW model enabled reliable extraction of dynamic

parameters despite beamline-induced oscillations in $|g_1(q, \Delta t)|^2$. Physically, $f(q)$ quantifies the fraction of density fluctuations at wavevector q that do not relax over the measurement window. A finite $f(q) > 0$ typically indicates dynamic arrest: particles are localized or caged over the corresponding length scale $\sim 2\pi/q$. Overall, the $g_1(q, \Delta t)$ function describes an exponential decay from unity to $f(q)$ at a relaxation rate $1/\tau(q)$, and modulated by the KWW exponent β, where $0 < \beta \leq 2$. Representative results for $|g_1(q, \Delta t)|^2$ illustrate both temporal (Fig. 4a) and wave vector (Fig. 4b) dependencies. The smooth curves are fits based on Equations 3 and 4. Shorter exposure times were necessary to minimize beam-induced damage and dynamics. This constraint led to poorer statistics at higher q (figs. S10−13). As a result, the autocorrelation function data are limited to the low-q regime, where q values remain below the SAXS peak position (Fig. 1e). In this range, the measured dynamics primarily reflect structural rearrangements within the growing fractal clusters that form the gel network.

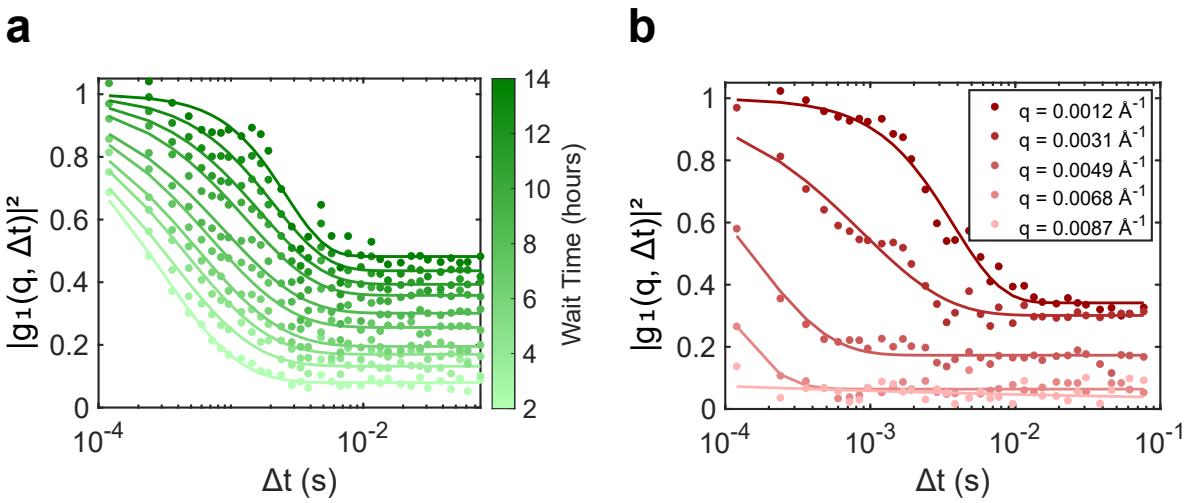

Fig. 4: Evolution of microscopic dynamics probed via XPCS. (a) Temporal (at $q = 0.0031\ ^{-1}$) and **(b)** q-dependent (at $t_w = 8.3$ hours) evolution of the normalized intensity autocorrelation function $|g_1(q, \Delta t)|^2$ for the evolving system. The smooth curves are fits based on Equations 3 and 4 to extract dynamic parameters. In both panels, $[\text{TBAPF}_6] = 0$ mM.

As expected, the characteristic relaxation time $\tau(q)$ increases with wait time, reflecting the progressive slowing of particle dynamics during gelation, with $\tau(q)$ rising rapidly after a period of modest change (Fig. 5a−b and figs. S14−17). At short wait times, the microscopic relaxation rate ($1/\tau(q)$) exhibits diffusive scaling with q^2, but as the system ages, it crosses over to a linear

q dependence, consistent with ballistic-like motion arising from collective rearrangements and internal stress relaxation (figs. S18 and S19) (*14, 16, 45, 49–56*). Concurrently, the KWW exponent β, which characterizes the distribution of relaxation times around $\tau(q)$, also remains nearly constant during a latency regime dominated by Brownian dynamics ($\beta \approx 1$), before exhibiting a transition to non-diffusive behavior as reflected in the deviation of β from 1 (Fig. 5c−d, and figs. S14−19) (*57*). The non-ergodicity parameter $f(q)$ increases steadily with time after an initial latency period, rising from $f(q) = 0$ (representing an equilibrium, fully diffusive state) to $f(q) = 1$ (indicating a fully arrested, non-ergodic state) (Fig. 5e−f, and figs. S14−17). A simplified picture is that the system comprises two coexisting populationsone dynamically arrested and one still undergoing free motion. A similar emergence of non-ergodicity has been observed in dynamic measurements of gels formed from larger charge-stabilized colloids after salt addition (*58*), as well as in marginal-solvent colloidal gels where gelation was triggered by temperature-induced attractions (*15, 34, 45, 48*). Notably, the latency period in the dynamic parameters shown here is similar to that observed in the evolution of ξ and D_f from the microstructure analysis (Fig. 2d−f) and also apparent in the optical evolution results (Fig. 3c−f). This delay suggests that the onset of dynamic arrest occurs only after substantial structural buildup, consistent with prior observations that rigidity in low-volume-fraction colloidal gels can emerge suddenly once compact clusters percolate (*59, 60*).

Mirroring the structural evolution observed via SAXS and optical spectroscopy, the time dependence of the gelation dynamics also exhibit a pronounced dependence on salt concentration. Beyond the latency point, the evolution of $\tau(q)$, $\beta(q)$, and $f(q)$ shifts systematically with increasing $TBAPF_6$ concentration, with curves translating horizontally in time while preserving their overall shape. This behavior indicates that salt accelerates the onset of dynamic evolution, apparently without altering the fundamental kinetic pathway. Consequently, rescaling the time axis by t_{10} collapses the data onto a single master curve, revealing a universal dynamic trajectory for the gelation process (Fig. 5b, d, f and figs. S14−17). In their investigation of thermo-reversible nanoparticle gels, Bahadur and coworkers (*34*) demonstrated that a single gel

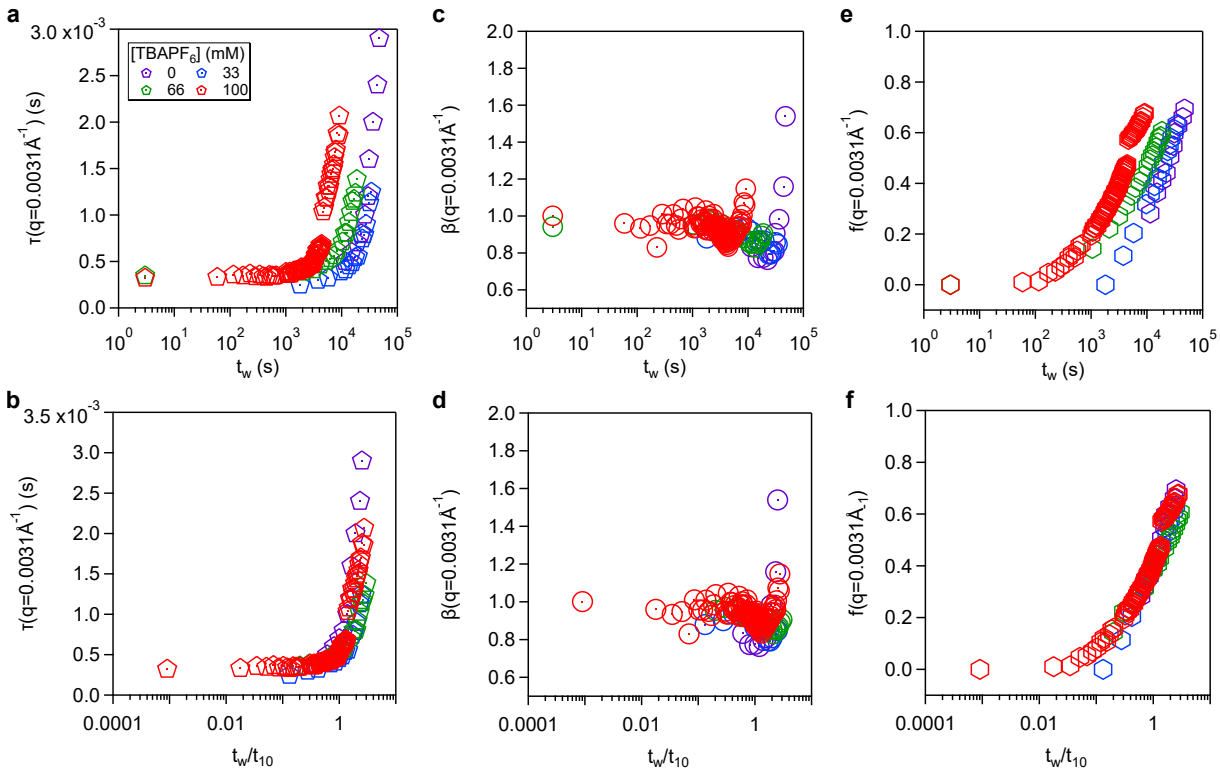

Fig. 5: Quantification of the microscopic NC dynamics. **(a)** Temporal evolution of the q-dependent characteristic relaxation time, $\tau(q)$. **(b)** $\tau(q)$ plotted against the gel-point-normalized wait time, t_w/t_{10}. **(c)(d)** Evolution of the KWW exponent, $\beta(q)$, with **(d)** showing $\beta(q)$ as a function of t_w/t_{10}. **(e)(f)** Evolution of the non-ergodicity parameter, $f(q)$, with **(f)** displaying $f(q)$ versus t_w/t_{10}. All data correspond to $q = 0.0031\,^{-1}$. The gel-point-normalized time, t_w/t_{10}, is defined as in Fig. 2a-b.

formation timescale collapses the structural, dynamical, and rheological responses across different formation times and quench temperatures. Consistent with this finding, our structural and dynamical results likewise exhibit such a collapse, underscoring the universality of the aggregation process. Importantly, beyond the collapse across t_w/t_{10}, we also observe a comparable timesalt superposition and universal progression when defining the characteristic time using alternative $S(0)$ thresholds. Thus, the universality of structural and dynamical evolution is not contingent upon the specific choice of structurally-defined characteristic time (fig. S20).

Additionally, although initially shown for a representative q, the time–salt superposition and universal progression of gelation are evident across the full range of experimentally accessible length scales, supporting the conclusion that a single salt-dependent mechanism governs both

local structuring and macroscopic network formation (Fig. 6 and fig. S19). To illustrate, we examine a q-dependent analysis of the temporal evolution of the non-ergodicity parameter, $f(q)$, which we model as:

$$f(q, t_w) = f_\infty(q) \left[1 - \exp\left(-\Gamma_f \left(t_w - t_0\right)\right)\right], \tag{5}$$

where $f_\infty(q)$ is the long-time localized fraction and Γ_f the growth rate of localization (*45*). Fits across scattering vectors q show that $f_\infty(q)$ decreases systematically with increasing q, indicating that large-scale density fluctuations become nearly arrested while small-scale fluctuations retain partial mobility, demonstrating that the gelation process exhibits both spatial and temporal heterogeneity. Notably, $f_\infty(q)$ collapses onto a universal curve across all salt concentrations (Fig. 6b), demonstrating convergence to the same long-time steady state at every q. The growth rate of the localized fraction Γ_f is also q-dependent, with higher salt concentrations driving faster localization (Fig. 6c). When normalized by the corresponding t_{10}, however, Γ_f values collapse onto a single curve, revealing universal length-scale dynamics across all salt conditions (Fig. 6d).

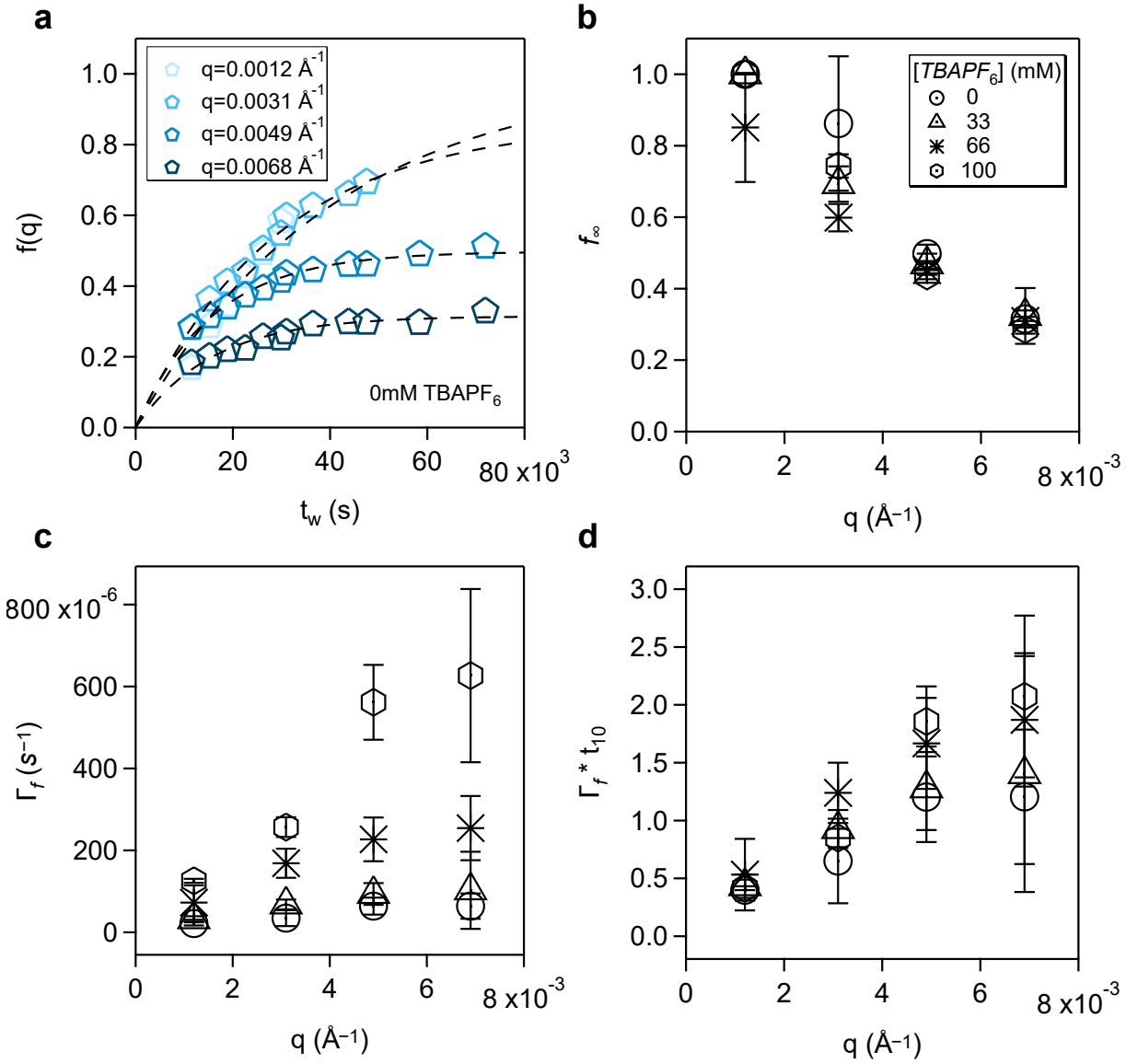

Fig. 6: Length-scale dependence of the emergence of non-ergodicity. **(a)** Non-ergodicity parameter $f(q)$ as a function of wait time t_w at several scattering wave vectors q, representing the probed length scales. The dashed lines are fits to Equation 5 for each q. Panels **b** and **c** show the fit results as a function of q. **(b)** Steady-state localized fraction at asymptotically large wait times, f_∞, shown as a function of q for all salt concentrations. **(c)** Localized growth rate, Γ_f, as a function of scattering vector q for all salt concentrations. The rate increases with salt across all q, with a more pronounced effect at higher q (smaller length scales). **(d)** The characteristic-time normalized localized growth rate $\Gamma_f * t_{10}$ as a function of q showing a superposition across length scales. In all panels, salt concentrations are indicated by different symbols: $\circ = 0$ mM, $\triangle = 33$ mM, $* = 66$ mM, and $\hexagon = 100$ mM.

Mechanism of Salt-Accelerated Gelation: Structural Insights

Given the time–salt superposition observed across length scales, probing the effects of salt on interactions and structuring at the smallest relevant scalethe NC core diameter σ_{core}offers insights into the mechanism of salt-accelerated gelation kinetics. To isolate the effect of salt, we first analyze the NC dispersion structure and effective pairwise interactions in the absence of attractive linkers. Upon ligand exchange to form AL-ITO NCs, structural analysis reveals pronounced differences in $S(q)$ compared to as-synthesized OL-ITO NCs. Specifically, $S(q)$ of AL-ITO NC dispersions exhibits stronger oscillations and decreased osmotic compressibility, as quantified by a smaller zero-wavenumber structure factor $S(0)$, relative to OL-ITO NCs at the same volume fraction and salt concentration (Fig. 7a, fig. S21). A pronounced drop in $S(q)$ below unity at low q and a shift of the primary peak to higher q with increasing Φ are hallmarks of long-range repulsion (Fig. 7b) (*61*). This behavior is consistent with charged, repulsive particles, where $S(q)$ can be modeled by Yukawa potentials for which the peak position follows $q_{\text{max}} \approx 2.2\rho^{1/3}$, with the number density ρ calculated as $\rho = \Phi/(\pi\sigma_{\text{core}}^3/6)$ (Fig. 7c) (*24, 62*). Zeta potential measurements confirm a high negative surface charge on the AL-ITO NCs (Fig. 7d, Table S1). Control experiments using PEG-phosphonic acid (molecular weight: 414 Da) as a capping ligandbearing a single phosphonic acid instead of a tri-carboxylic acidyielded NC dispersions with $S(q)$ lacking the correlation peak oscillations of charged colloids and a zeta potential value near 0 mV, consistent with AL-ITOs negative surface charge originating from the abundant carboxylic acid groups, which may undergo deprotonation (fig. S22).

Salt addition increases the ionic strength and reduces the electrostatic double-layer thickness, thereby screening interparticle repulsions. This screening effect is evident in the evolution of $S(q)$ with increasing salt concentration at fixed Φ. As ionic strength rises, low-q intensity increases and the correlation peak decreases in magnitude, broadens, and shifts to higher q, indicating that particles can approach each other more closely. These trends are consistent with a reduced long-range repulsion between NCs. Since there is no appreciable attraction, a colloidal 'gas'-like structure is approached (Fig. 7e), similar to that observed for sterically-stabilized OL-

ITO NCs. To quantify the screening effect of the salt on the pairwise interactions, we calculate the osmotic second virial coefficient B_2 from the osmotic compressibility, which relates to $S(0)$ as:

$$\frac{1}{S(0)} - 1 = (k_B T)^{-1} \left(\frac{\partial \Pi}{\partial \rho} \right)_T - 1 = 2B_2\rho + \mathcal{O}(\rho^2), \tag{6}$$

where Π is the osmotic pressure. By fitting a quadratic function to $S(q)$ at low q, we extract $S(0)$ (Fig. 7f, inset, and fig. S23) and estimate B_2 (Fig. 7f) (*61,63,64*). The observed monotonic decrease in B_2 with increasing salt confirms that salt screens repulsive pairwise interactions. The salt-induced reduction in effective pairwise NC repulsion is most pronounced at low salt concentrations ($0 < [\text{TBAPF}_6] < 33$ mM). Above this range, B_2 remains positive and nearly constant, indicating that the dispersion remains net repulsive due to the steric effects of the ligands, consistent with observations for for OL-ITO (*63*).

Assuming interparticle interactions follow DerjaguinLandauVerweyOverbeek (DLVO) theory (*65, 66*), we fit the experimental salt-dependence of B_2 using its integral expression to extract the NC charge number Z and thermodynamic hard-sphere diameter σ_{HS} (fig. S24). To minimize the influence of adventitious counterions on the estimated screening length, fitting was restricted to systems with salt concentrations ≥ 3 mM, where added salt dominates the ionic strength. From this analysis, we obtained $Z = 71 \pm 6$ and $\sigma_{\text{HS}} = 19.4 \pm 1.9$ nm. Using these parameters, structure factors computed via integral equation theory showed qualitative agreement with experimental $S(q)$ (fig. S25). This agreement, along with the quantitative trends in B_2, confirms that added salt screens interparticle repulsions. Screening reduces the configurational constraints of the electrostatic repulsions, which could facilitate faster local structure evolution, thereby enhancing gelation kinetics upon introduction of chemical linkers. However, the fact that the reduction in effective repulsion is most pronounced at low salt concentrations suggests that electrostatic screening alone cannot account for the continued acceleration of gelation across the full $0 - 100$ mM salt range.

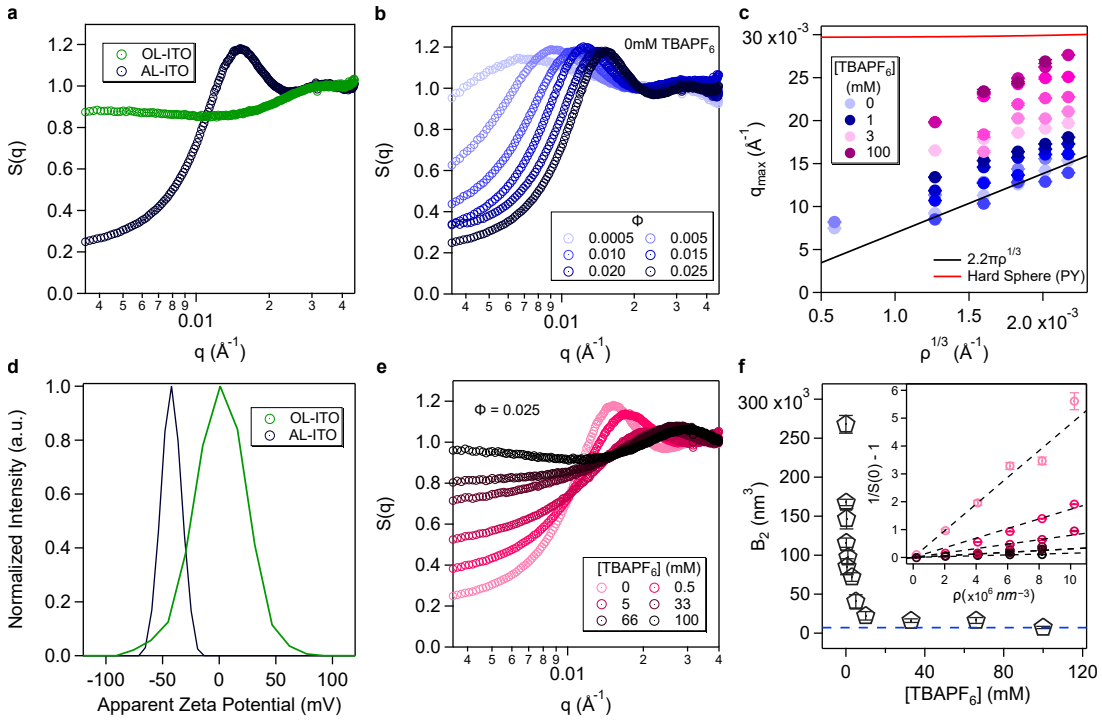

Fig. 7: Salt effect on effective pairwise interactions of dispersed NCs. (a) $S(q)$ of 16.8 nm AL-ITO NC dispersions at $\Phi = 0.025$ with no added salt and with different surface ligands (oleate-capped, OL vs aldehyde-capped, AL) **(b)** $S(q)$ of AL-ITO NCs in DMF at different colloid volume fractions ($0.0005 \leq \Phi \leq 0.025$) dispersed in DMF with no added salt. **(c)** Plot of q_{max} versus experimental number density $\rho^{1/3}$ at increasing salt concentrations from 0–100 mM. The solid black line, $q_{\text{max}} = 2.2\pi\rho^{1/3}$, indicates behavior theoretically expected from charged colloids with long-range repulsions that maximize interparticle spacing (*24, 62*). The red curve represents the exact solution of the Percus-Yevick integral equation for a hard-sphere fluid at a packing fraction consistent with ρ and a hard-sphere diameter σ_{HS} obtained from a fit to the experimental second osmotic virial coefficient B_2 vs salt results (see fig. S23). The legend lists only a subset of the data to represent the range of salt concentrations studied. **(d)** Zeta potential measurement of OL-ITO and AL-ITO NCs ($\Phi = 0.005$) in toluene and DMF, respectively, without added salt. **(e)** $S(q)$ of AL-ITO NCs in DMF with increasing salt concentration $0 \leq$ [TBAPF$_6$] ≤ 100 mM at constant colloid volume fraction $\Phi = 0.025$. **(f)** Osmotic second virial coefficient B_2 as a function of [TBAPF$_6$]. The dotted blue line represents B_2 for the neutral OL-ITO NC dispersion system. The inset shows the reciprocal of the structure factor at zero wavevector, $1/S(0)$, versus NC number density ρ, at different salt concentrations. The osmotic second virial coefficient B_2 is calculated as one-half the slope of the linear regression (Equation 6), shown as the dashed black lines. The data points in the inset are color-coded to match the legend in **(e)**

Kinetic Monte Carlo (kMC) simulations (*67*) (see Materials and Methods and Supplementary Information) offer one avenue for investigating how electrostatic interactions and salt screening may be expected to influence linked colloidal gelation, and whether salt screening is a primary mechanism accelerating the dispersion-to-gel evolution. The interparticle interactions are described by the DLVO potential, with the Debye length determined by the salt concentration. The simulations and corresponding $S(q)$ reproduce key features of the experimental data, showing increased NC coordination upon network formation (Fig. 8a) and subsequent coarsening into denser structures, quantified by the increase in ΔS (the difference between the primary contact peak and the Porod dip in $S(q)$, Fig. 8b). We use ΔS as the measure of structural evolution in place of $S(0)$, as the resolution of $S(q)$ in the low-q region is restricted by the finite size of the simulations. Tracking ΔS over simulation time confirms salt-accelerated gelation and coarsening rates (Fig. 8c). When $\Delta S \geq 1.2$, the ΔS-log(t_w) curve shows a nonlinear saturation trend, indicating that the kinetics of coarsening attenuates. Hence, we choose to use the simulation time at which $\Delta S = 1.2$ as the characteristic time ($t_{1.2}$). We find that $t_{1.2}$ decreases with increasing salt concentration, albeit in a nonlinear fashion (Fig. 8d). Similar trends are observed when defining gelation based on other ΔS thresholds, confirming the robustness of this observation (fig. S26). Notably, $t_{1.2}$ drops sharply between 10 and 33 mM, then levels off from 33 to 100 mMmirroring the plateau in B_2 and the saturation of the Yukawa potential at high salt concentrations (fig. S27).

Despite the nonlinear dependence of the characteristic time on salt concentration, the simulated static structure factors at $t_{1.2}$ exhibit approximate self-similarity, consistent with the experimental observations (Fig. 2a, inset). Minor deviations appear only in the low-q region (Fig. 8d, inset; fig. S26), reinforcing that the mesoscale gel structure at this stage is largely independent of salt concentration. This structure universality further justifies the use of ΔS as a representative metric for structural evolution. Normalizing the time axis by $t_{1.2}$ yields approximate timesalt superposition in the $\Delta S(t_w)$ trajectories (Fig. 8e). However, the quality of the trajectory collapse depends on the choice of ΔS used to define the characteristic time. Better superposition

at early times is achieved with lower ΔS thresholds (e.g., $\Delta S = 1.1$), whereas later times align better with higher thresholds (e.g., $\Delta S = 1.4$; fig. S26).

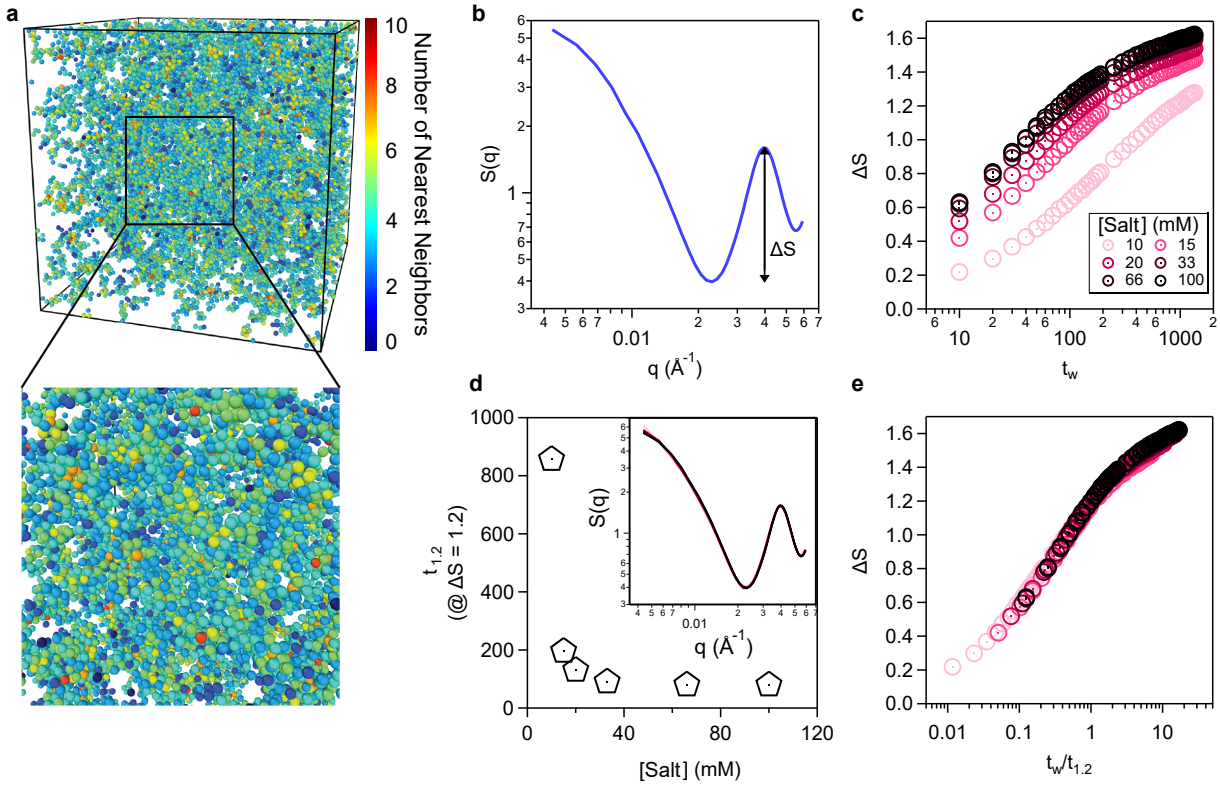

Fig. 8: Simulation of salt-accelerated gelation. **(a)** Snapshot of the colloidal gel from a kinetic Monte Carlo simulation. NC colors indicates their number of nearest neighbors. **(b)** Schematic $S(q)$ illustrating the definition of ΔS, which grows as the colloidal network evolves. **(c)** ΔS as a function of waiting time for different salt concentrations. **(d)** $t_{1.2}$ versus salt concentration; the characteristic time is defined as the time when ΔS reaches 1.2. Inset shows the $S(q)$ of colloidal gels at $t_{1.2}$ for various salt concentrations. **(e)** Timesalt superposition shown by plotting ΔS against normalized waiting time.

The predicted nonlinear dependence of characteristic time $t_{1.2}$ on salt concentration, taken together with the reduced effects of electrostatic screening observed for B_2 at high salt concentration, indicate that electrostatic screening alone cannot explain the accelerated gelation kinetics across the full $0 - 100$ mM salt concentration window. While DLVO theory provides a useful approximate framework, its simplifying assumptions lose validity outside of the dilute regime for both colloids and electrolytes. Moreover, the kinetic Monte Carlo simulations neglect other interactions known to influence colloidal gelation, such as many-body hydrodynamic forces (*68, 69*). Furthermore, we have neglected charge regulationthe process by which a

particles surface charge adjusts dynamically in response to changes in the surrounding chemical environment (*70*). This phenomenon may be relevant to our system; we find that the charge number Z that best matches experimental $S(q)$ with theoretical structure factors from integral equation theory varies with both salt concentration and colloid volume fraction (figs. S28–S29, Table S2). Despite these shortcomings, the ability of DLVO theory and kinetic Monte Carlo simulations to qualitatively capture salt-accelerated gelation kinetics and salt-time superposition effects suggest they are helpful starting point for interpreting the experimental observations.

Mechanism of Salt-Accelerated Gelation: Reaction-Driven Insights

To examine other factors that may be influencing the salt-accelerated gelation beyond electrostatic screening of the colloids, we investigated the underlying chemical linking process: the hydrazone condensation reaction. A simplified molecular model was designed using benzaldehyde and benzoylhydrazine, reacted under the same solvent conditions as the NC gelation system, with benzaldehyde as the limiting reagent (Fig. 9a). Chemical linking kinetics were assessed while $TBAPF_6$ salt concentrations were varied from 0 to 66 mM. Using ^{1}H NMR spectroscopy (Fig. 9b), we monitored the consumption of reactants and formation of the hydrazone product over 23 hours (figs. S3033). Integration of characteristic benzaldehyde and hydrazone peaks enabled calculation of the reaction rate constant k using the integrated second-order rate law (*71, 72*):

$$\frac{1}{[B]_0 - [A]_0} \ln\left(\frac{[A]_0[B]}{[B]_0[A]}\right) = kt \tag{7}$$

where $[A]_0$ and $[B]_0$ are the initial concentrations of benzaldehyde and benzoylhydrazine, $[A]$ and $[B]$ are their concentrations at time t, and k is extracted as the slope of the linear regression (fig. S34). The variations in k as a result of added salt are a model to reflect the rate of bond formation between the NCs, but in a reaction environment more amenable to quantification. The values of k were derived using spectral data up to $80\ (\pm 3)\ \%$ of the time required to reach a steady-state product concentration. We observed that the time to 80% completion decreases with increasing salt concentration (Fig. 9c), mirroring the trends in t_{10} and $t_{0.5}$ from SAXS and

UV-Vis results, respectively (Figs. 2b and 3b). Accordingly, k increases with salt concentration, suggesting that increased ionic strength, achieved through the addition of the salt, enhances the condensation reaction rate-possibly by stabilizing the charged intermediates created during the condensation reaction. Notably, the salt acceleration of the linking reaction rate continues to grow in magnitude, even at higher salt concentrations where electrostatic screening effects on B_2 have saturated.

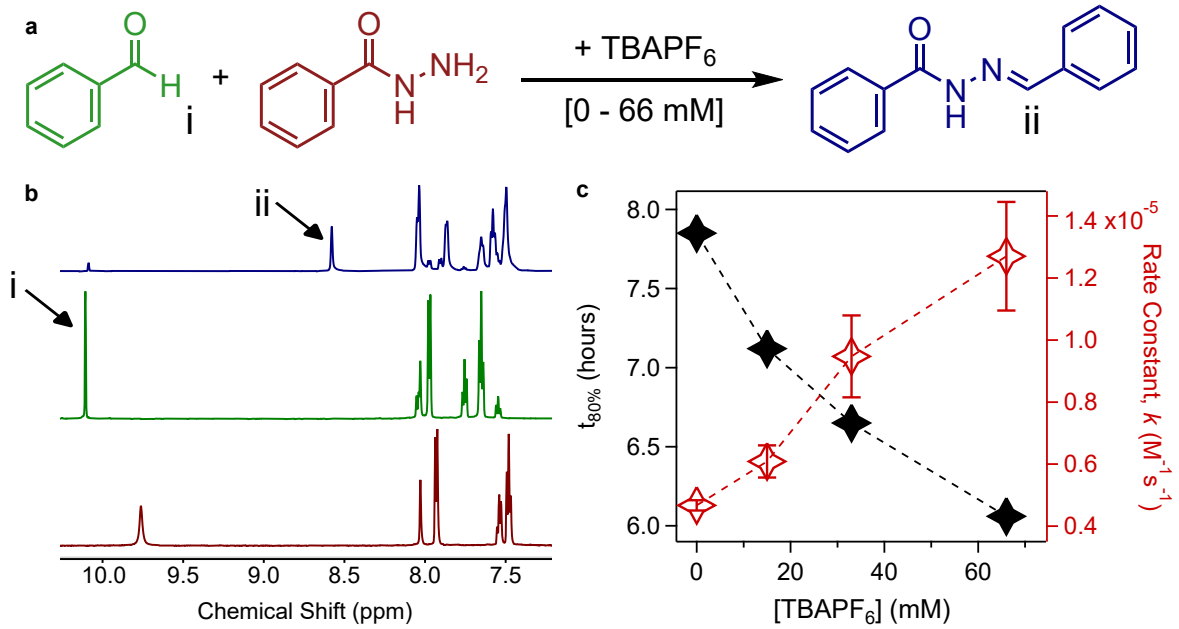

Fig. 9: Salt effect on kinetics of hydrazone bond formation. **(a)** Schematic of the chemical reaction resulting in hydrazone bond formation from reactants, benzaldehyde and benzoylhydrazine with varied [$TBAPF_6$]. **(b)** Representative ^{1}H-NMR spectra of the hydrazone bonded product, benzaldehyde reactant, and benzoylhydrazine reactant (from top to bottom) in the region of interest used to track the kinetics of bond formation. Peak i at ~ 10.1 ppm corresponds to the aldehyde proton in benzaldehyde and peak ii at ~ 8.6 ppm corresponds to the imine proton in the hydrazone product. **(c)** Time of 80% reaction completion (black data points) and rate of linking reaction, k, (red data points) with respect to concentration of $TBAPF_6$. Error bars on the k values represent 95% confidence interval of the standard fitting errors (see fig. S34).

These measurements of the reaction rate constant, when viewed alongside the structural characterization of the NC dispersions and the simulations of gelation kinetics, reveal a multimodal mechanism by which salt accelerates gelation. At low concentrations, salt screens electrostatic repulsions, lowering the free energy barrier for the NCs to approach one another. Once within close proximity, hydrazone bond formation initiates network assembly. While

electrostatic screening saturates at relatively low salt concentrations, the rate of chemical bond formation continues to increase with salt concentration, enabling faster linking interactions between multiple NCs, consequently accelerating gelation.

DISCUSSION

The observations of time–salt superposition of linked NC gel formation reported here relate to broader analyses of time–composition superposition in diverse soft matter systems, including spontaneously aging Laponite suspensions (*19*), protein condensates (*20*), polymer hydrogels (*21*), polyelectrolyte complexes (*22*), and colloidal gels (*34, 36, 73–75*). In many cases, changing composition modifies physical interactions in a way that impacts time-dependent structure and corresponding properties, and the results are examined through techniques like rheology that probe the macroscopic mechanical response under deformation. Our work provides mechanistic insight by connecting microscopic structure and dynamics to corresponding evolution of macroscopic observables, advancing understanding by integrating experimental and computational approaches that probe chemistry, structure, and dynamics across length scales.

By tracing the gelation pathway across a wide salt concentration range using complementary techniquesSAXS, optical spectroscopy, XPCS, kinetic NMR, and kinetic Monte Carlo simulationswe establish that salt accelerates colloidal network formation and dynamic evolution without altering the final gel structure. The observed time–salt superposition of structural and dynamical data across scales highlights a universal pathway along which salt enhances the kinetic progression. Effective pairwise interaction measurements and simulations confirm that electrostatic screening lowers repulsive barriers to assembly, enabling particle approach, albeit with the largest changes occurring within the low salt concentration regime. Simultaneously, NMR studies demonstrate that salt also accelerates the hydrazone bond formation kinetics, likely through enhanced proton transfer in a more polar environment. Despite the success of DLVO theory and kinetic Monte Carlo simulations as an initial framework to describe these observations, its lim-

itationsincluding neglect of charge regulation, many-body thermodynamic and hydrodynamic interactions, and salt-dependent chemical reaction ratessuggest future efforts should aim to incorporate these complexities into models for a more complete description of gelation dynamics. On the experimental side, expanding control parameters beyond saltsuch as pH, solvent properties, and particle charge densityoffers additional avenues to finely tune particle interactions and gelation kinetics. Ultimately, integrating these insights will help in the rational design of new soft materials including reconfigurable, programmable colloidal NC architectures with tailored mechanical and dynamic behaviors, and optical response.

MATERIALS AND METHODS

Ligand Synthesis

Aldehyde-terminated ligands (**AL**) were synthesized by modifying established literature methods (*8*). Briefly, a peptide base was synthesized using solid phase peptide synthesis (SPPS), with the aldehyde functional group added via solid phase-copper azide alkyne cycloaddition (SP-CuAAC). The resulting ligand was then cleaved from the resin, purified using high performance liquid chromatography, then dried for use.

Synthesis and Functionalization of NCs

ITO NCs were synthesized on a Schlenk line through a modification of a slow growth procedure (*29*). A precursor solution containing Sn(IV)acetate and In(III)acetate in 10 mL oleic acid was degassed (90 °C, 1 hour) and heated (150 °C, 3 h) under flowing nitrogen. The solution was then slowly injected into 13 mL oleyl alcohol at 290 C under nitrogen flow. After synthesis, NCs were washed five times with ethanol and dispersed in hexane. The NCs were functionalized through a direct ligand exchange (*8, 17*). As-synthesized, oleate-capped NCs were precipitated into a pellet and sonicated in a ligand solution (0.01 M **AL** in DMF) for 2 hours before reacting overnight. The functionalized NCs were washed three times with a 3:7 (v:v) EtOH:hexane mixture and then dispersed in pure DMF.

Preparation of Samples for Scattering and Spectroscopic Measurements

SAXS and XPCS: SAXS measurements were performed in transmission mode at three facilities: the SAXSLAB Ganesha instrument at the Texas Materials Institute (TMI), University of Texas at Austin; beamline CHX (11-ID) at the National Synchrotron Light Source II (NSLS-II, Upton, NY, USA); and sector 8-ID-I at the Advanced Photon Source (APS, Argonne, IL, USA), with sample-to-detector distances of $\sim$ 1, 16, and 9 m, respectively. XPCS was conducted at CHX using a 12.8 keV beam focused to 40×40 μm^2, with scattering patterns collected on a Dectris Eiger 500K area detector (pixel size 75×75 μm^2) with a maximum frame rate of

9 kHz positioned 16 m from the sample. After a dose-dependence study (fig. S36), each XPCS series was recorded at full transmission with 1000 frames. At this setting, the short exposure time minimized beam-induced dynamics despite the high transmission. All the data presented here were recorded at a frame rate of 9 kHz. All samples, including a silver behenate standard for q-calibration (TMI SAXS), were sealed in flame-closed 1 mm glass capillaries (Hampton Research) with approximately 10 micron wall thickness. SAXS data were processed using the Irena and Nika packages in Igor Pro. XPCS data analysis was done using custom python code for data access and reduction in ipython notebooks running on Jupyter Lab provided by the beamline.

Optical Spectroscopy: Gel optical spectra were measured with an Agilent Cary 5000 UV-Vis-NIR spectrophotometer over a wavenumber range of $4000 - 8000$ cm^{-1}. Gel precursors were injected into a custom cells made from two glass slides separated by a Surlyn thermoadhesive spacer with a 25 micron thickness. The cells were placed horizontally in the path of a columnated beam between two fiber optic cables. Cell construction and optical measurement setup is shown in fig. S37. Gels were measured at varying time intervals to ascertain high-time-resolution spectral evolution. Normalized optical spectra of gels at each salt concentration can be found in fig. S6. The peak positions were fit with a gaussian fitting of the highest 10% of data points, and the the FWHM values were calculated using the discrete wavenumber width of half the peak value. Peak evolutions with time were fit with a decreasing standard logistic function, while FWHM were fit with an increasing standard logistic function. The time axes of the curves were normalized by the fit $t_{0.5}$ to evaluate the time–salt superimposition of optical properties.

NMR: Nuclear Magnetic Resonance (NMR) measurements were performed using a Bruker OXO-500 spectrometer using a cryoprobe. Spectra were calibrated to the DMF solvent peaks. Samples were prepared in a 75:25 vol/vol% of DMF-d7: ethylene glycol-d6 solvent mixture, containing 20 mM benzaldehyde, 22 mM benzoylhydrazine, 1,3,5-trimethoxybenzene as an internal standard, and a varied concentration of $TBAPF_6$ of 0, 15, 33, or 66 mM. Peak integrals

and calculated concentrations of the reaction were normalized to the internal standard.

DLS and Zeta Potential: Dynamic light scattering (DLS) measurements of dilute NCs ($\Phi = 0.0005$) were performed using a Zetasizer Nano ZS (Malvern) with a He-Ne laser ($\lambda = 633$ nm) and 173° back-scattering detection at 25°C. Autocorrelation functions were collected in triplicate (10 s each) and averaged. Diffusion coefficients were obtained from the short-time decay using third-order cumulant analysis, and hydrodynamic diameters were calculated via the StokesEinstein equation. Zeta potential (ZP) was measured using the same instrument and conditions, with a dip cell in a glass cuvette. Measurements were repeated at least three times for reproducibility. Both DLS and ZP results can be found in Table S1.

Numerical Fitting and Calculation of the Structural Factors of the Dispersions

We computed structure factors for NCs interacting via the DLVO potential using liquid-state integral equation theory (IET) (*76*). We numerically solved the Ornstein-Zernike equation with the hypernetted chain (HNC) closure implemented in the pyPRISM package (v1.0.4) (*77*). To validate the applicability of IET for this system, we performed Brownian dynamics (BD) simulations using the Highly Optimized Object-oriented Many-particle Dynamics-Blue Edition (HOOMD-Blue, v4.5.0) toolkit (*78*) to model NCs with DLVO-type interactions. The hard-sphere interactions in BD simulations is approximated using the Heyes-Melrose potential (*79*). Comparison between IET predictions and BD simulation results ensures consistency across theoretical and computational approaches (fig. S35). Additional details on the structure factor calculations are provided in the Supplementary Materials.

Kinetic Monte Carlo Simulations of the Gelation Process

The gelation process is simulated with customized kinetic Monte Carlo (kMC) simulations (*67*). Details of the kMC simulations are provided in the Supplementary Materials. Static structural factors are calculated from snapshots of kMC simulations using the Freud package (*80*).

Kinetics of Chemical Linking: Further details of the sample preparation and the second-order reaction integrated rate law calculations and the linear regression can be found in the supplementary materials.

ACKNOWLEDGMENTS

We acknowledge the Texas Advanced Computing Center (TACC) at The University of Texas at Austin for providing HPC resources. This research used resources at the CHX beamline of the National Synchrotron Light Source II, a U.S. Department of Energy (DOE) Office of Science User Facility operated for the DOE Office of Science by Brookhaven National Laboratory under Contract No. DE-SC0012704. Additionally, aspects of this research was performed on APS beam time award (DOI: https://doi.org/10.46936/APS-188726/60013713) from the Advanced Photon Source, a U.S. Department of Energy (DOE) Office of Science user facility operated for the DOE Office of Science by Argonne National Laboratory under Contract No. DE-AC02-06CH11357. We are grateful to Drs. Suresh Narayanan and Qingteng Zhang for their help with data collection.

Funding: This work was primarily supported by the National Science Foundation (NSF) through the Center for Dynamics and Control of Materials: an NSF MRSEC under Cooperative Agreement No. DMR-2308817 and under an NSF DMREF project, CBET-2323482. TMT acknowledges support from the Army Research Office under Grant Number W911NF-23-1-0387 and DJM acknowledges support from NSF under CHE-2303296. This work was also supported by the Welch Foundation (Grant Nos. F-1696 and F-1848).

Competing Interests: All authors declare no competing interests.

Data and Materials Availability: All data needed to evaluate the conclusions in the paper are present in the paper and/or the Supplementary Materials.

REFERENCES AND NOTES

1. I. Kriegel, F. Scotognella, L. Manna, Plasmonic Doped Semiconductor Nanocrystals: Properties, Fabrication, Applications and Perspectives. *Phys. Rep.* **674**, 1–52 (2017).

2. A. Agrawal, S. H. Cho, O. Zandi, S. Ghosh, R. W. Johns, D. J. Milliron, Localized surface plasmon resonance in semiconductor nanocrystals. *Chem. Rev.* **118**, 3121-3207 (2018). PMID: 29400955.

3. S. K. Ghosh, T. Pal, Interparticle coupling effect on the surface plasmon resonance of gold nanoparticles: From theory to applications. *Chem. Rev.* **107**, 4797-4862 (2007). PMID: 17999554.

4. A. Klinkova, R. M. Choueiri, E. Kumacheva, Self-assembled plasmonic nanostructures. *Chem. Soc. Rev.* **43**, 3976-3991 (2014).

5. N. S. Mueller, Y. Okamura, B. G. M. Vieira, S. Juergensen, H. Lange, E. B. Barros, F. Schulz, S. Reich, Deep strong lightmatter coupling in plasmonic nanoparticle crystals. *Nature* **583**, 780–784 (2020).

6. C. A. Saez Cabezas, G. K. Ong, R. B. Jadrich, B. A. Lindquist, A. Agrawal, T. M. Truskett, D. J. Milliron, Gelation of plasmonic metal oxide nanocrystals by polymer-induced depletion attractions. *Proc. Natl. Acad. Sci. U.S.A.* **115**, 8925-8930 (2018).

7. A. M. Green, C. K. Ofosu, J. Kang, E. V. Anslyn, T. M. Truskett, D. J. Milliron, Assembling inorganic nanocrystal gels. *Nano Lett.* **22**, 1457-1466 (2022).

8. M. N. Dominguez, M. P. Howard, J. M. Maier, S. Valenzuela, Z. M. Sherman, L. C. Reimnitz, J. Kang, S. H. Cho, S. L. Gibbs, A. K. Menta, D. L. Zhuang, A. van der Stok, S. J. Kline, E. V. Anslyn, T. M. Truskett, D. J. Milliron, Assembly of linked nanocrystal colloids by reversible covalent bonds. *Chem. Mater.* **32**, 10235–10245 (2020).

9. J. Kang, S. A. Valenzuela, E. Y. Lin, M. N. Dominguez, Z. M. Sherman, T. M. Truskett, E. V. Anslyn, D. J. Milliron, Colorimetric quantification of linking in thermoreversible nanocrystal gel assemblies. *Sci. Adv.* **8**, eabm7364 (2022).

10. P. Rusch, D. Zmb, N. C. Bigall, Control over structure and properties in nanocrystal aerogels at the nano-, micro-, and macroscale. *Acc. Chem. Res.* **53**, 2414-2424 (2020). PMID: 33030336.

11. F. Matter, A. L. Luna, M. Niederberger, From colloidal dispersions to aerogels: How to master nanoparticle gelation. *Nano Today* **30**, 100827 (2020).

12. Z. M. Sherman, A. M. Green, M. P. Howard, E. V. Anslyn, T. M. Truskett, D. J. Milliron, Colloidal nanocrystal gels from thermodynamic principles. *Acc. Chem. Res.* **54**, 798-807 (2021).

13. S. M. Morozova, L. Lpez-Flores, A. Gevorkian, H. Zhang, V. Adibnia, W. Shi, D. Nykypanchuk, T. G. Statsenko, G. C. Walker, O. Gang, M. O. de la Cruz, E. Kumacheva, Colloidal clusters and networks formed by oppositely charged nanoparticles with varying stiffnesses. *ACS Nano* **17**, 15012-15024 (2023). PMID: 37459253.

14. A. Jain, F. Schulz, I. Lokteva, L. Frenzel, G. Grbel, F. Lehmkhler, Anisotropic and heterogeneous dynamics in an aging colloidal gel. *Soft Matter* **16**, 2864-2872 (2020).

15. Y. Chen, Q. Zhang, S. Ramakrishnan, R. L. Leheny, Memory in aging colloidal gels with time-varying attraction. *J. Chem. Phys.* **158**, 024906 (2023).

16. L. Cipelletti, S. Manley, R. C. Ball, D. A. Weitz, Universal aging features in the restructuring of fractal colloidal gels. *Phys. Rev. Lett.* **84**, 2275–2278 (2000).

17. Z. M. Sherman, K. Kim, J. Kang, B. J. Roman, H. S. N. Crory, D. L. Conrad, S. A. Valenzuela, E. Lin, M. N. Dominguez, S. L. Gibbs, E. V. Anslyn, D. J. Milliron, T. M. Truskett, Plasmonic response of complex nanoparticle assemblies. *Nano Lett.* **23**, 3030-3037 (2023). PMID: 36989531.

18. E. D. Gado, W. Kob, Structure and relaxation dynamics of a colloidal gel. *Europhys. Lett.* **72**, 1032 (2005).

19. W. Sun, Y. Yang, T. Wang, H. Huang, X. Liu, Z. Tong, Effect of adsorbed poly(ethylene glycol) on the gelation evolution of laponite suspensions: Aging time-polymer concentration superposition. *J. Colloid Interface Sci.* **376**, 76-82 (2012).

20. N. D. Anthuparambil, S. Timmermann, M. Dargasz, S. Retzbach, M. D. Senft, N. Begam, A. Ragulskaya, M. Paulus, F. Zhang, F. Westermeier, M. Sprung, F. Schreiber, C. Gutt, Salt induced slowdown of kinetics and dynamics during thermal gelation of egg-yolk. *J. Chem. Phys.* **161**, 055102 (2024).

21. X. Li, F. Luo, T. L. Sun, K. Cui, R. Watanabe, T. Nakajima, J. P. Gong, Effect of salt on dynamic mechanical behaviors of polyampholyte hydrogels. *Macromolecules* **56**, 535-544 (2023).

22. E. Spruijt, J. Sprakel, M. Lemmers, M. A. C. Stuart, J. van der Gucht, Relaxation dynamics at different time scales in electrostatic complexes: Time-salt superposition. *Phys. Rev. Lett.* **105**, 208301 (2010).

23. J. C. F. Toledano, F. Sciortino, E. Zaccarelli, Colloidal systems with competing interactions: from an arrested repulsive cluster phase to a gel. *Soft Matter* **5**, 2390-2398 (2009).

24. J. A. Bollinger, T. M. Truskett, Fluids with competing interactions. I. Decoding the structure factor to detect and characterize self-limited clustering. *J. Chem. Phys.* **145**, 064902 (2016).

25. J. A. Bollinger, T. M. Truskett, Fluids with competing interactions. II. Validating a free energy model for equilibrium cluster size. *J. Chem. Phys.* **145**, 064903 (2016).

26. J. Opdam, M. Tateno, H. Tanaka, Unraveling the impact of competing interactions on nonequilibrium colloidal gelation. *ACS Nano* **19**, 2151521524 (2025). PMID: 40414685.

27. Y. Chen, S. A. Rogers, S. Narayanan, J. L. Harden, R. L. Leheny, Microscopic ergodicity breaking governs the emergence and evolution of elasticity in glass-forming nanoclay suspensions. *Phys. Rev. E* **102**, 042619 (2020).

28. O. Czakkel, A. Madsen, Evolution of dynamics and structure during formation of a cross-linked polymer gel. *Europhys. Lett.* **95**, 28001 (2011).

29. A. W. Jansons, J. E. Hutchison, Continuous growth of metal oxide nanocrystals: Enhanced control of nanocrystal size and radial dopant distribution. *ACS Nano* **10**, 6942–6951 (2016).

30. B. Butler, H. Hanley, D. Hansen, D. Evans, Aggregation of a quenched lennard-jones system under shear. *Phys. Rev. B* **53**, 2450 (1996).

31. M. E. Fisher, The theory of equilibrium critical phenomena. *Rep. Prog. Phys.* **30**, 615 (1967).

32. E. Zaccarelli, S. V. Buldyrev, E. La Nave, A. J. Moreno, I. Saika-Voivod, F. Sciortino, P. Tartaglia, Model for reversible colloidal gelation. *Phys. Rev. Lett.* **94**, 218301 (2005).

33. B. A. Lindquist, R. B. Jadrich, D. J. Milliron, T. M. Truskett, On the formation of equilibrium gels via a macroscopic bond limitation. *J. Chem. Phys.* **145**, 074906 (2016).

34. D. Bahadur, Q. Zhang, E. M. Dufresne, P. Grybos, P. Kmon, R. L. Leheny, P. Maj, S. Narayanan, R. Szczygiel, J. W. Swan, A. Sandy, S. Ramakrishnan, Evolution of structure and dynamics of thermo-reversible nanoparticle gelsa combined xpcs and rheology study. *J. Chem. Phys.* **151**, 104902 (2019).

35. N. D. Anthuparambil, A. Girelli, S. Timmermann, M. Kowalski, M. S. Akhundzadeh, S. Retzbach, M. D. Senft, M. Dargasz, D. Gutmller, A. Hiremath, M. Moron, . ztrk, H.-F. Poggemann, A. Ragulskaya, N. Begam, A. Tosson, M. Paulus, F. Westermeier, F. Zhang, M. Sprung, F. Schreiber, C. Gutt, Exploring non-equilibrium processes and spatio-temporal scaling laws in heated egg yolk using coherent x-rays. *Nature Communications* **14**, 5580 (2023).

36. M. Y. Lin, H. M. Lindsay, D. A. Weitz, R. C. Ball, R. Klein, P. Meakin, Universality in colloid aggregation. *Nature* **339**, 360–362 (1989).

37. J. Kang, Z. M. Sherman, D. L. Conrad, H. S. Crory, M. N. Dominguez, S. A. Valenzuela, E. V. Anslyn, T. M. Truskett, D. J. Milliron, Structural control of plasmon resonance in molecularly linked metal oxide nanocrystal gel assemblies. *ACS Nano* **17**, 24218–24226 (2023).

38. A. M. Green, S. Kadulkar, Z. M. Sherman, T. M. Fitzsimons, C. K. Ofosu, J. Yan, D. Zhao, J. Ilavsky, A. M. Rosales, B. A. Helms, V. Ganesan, T. M. Truskett, D. J. Milliron, Depletion-driven assembly of polymer-coated nanocrystals. *J. Phys. Chem. C* **126**, 19507-19518 (2022).

39. Z. M. Sherman, D. J. Milliron, T. M. Truskett, Distribution of single-particle resonances determines the plasmonic response of disordered nanoparticle ensembles. *ACS Nano* **18**, 21347–21363 (2024).

40. A. M. Green, W. J. Chang, Z. M. Sherman, Z. Sakotic, K. Kim, D. Wasserman, D. J. Milliron, T. M. Truskett, Structural order and plasmonic response of nanoparticle monolayers. *ACS Photonics* **11**, 1280–1292 (2024).

41. R. L. Leheny, XPCS: Nanoscale motion and rheology. *Curr. Opin. Colloid Interface Sci.* **17**, 3-12 (2012).

42. A. R. Sandy, Q. Zhang, L. B. Lurio, Hard x-ray photon correlation spectroscopy methods for materials studies. *Annu. Rev. Mater. Res* **48**, 167-190 (2018).

43. A. Madsen, A. Fluerasu, B. Ruta, Structural dynamics of materials probed by x-ray photon correlation spectroscopy. *Synchrotron Light Sources and Free-Electron Lasers: Accelerator Physics, Instrumentation and Science Applications*, E. J. Jaeschke, S. Khan, J. R. Schneider, J. B. Hastings, eds. (Springer International Publishing, Cham, 2020), pp. 1989–2018.

44. F. Lehmkhler, W. Roseker, G. Grbel, From femtoseconds to hoursmeasuring dynamics over 18 orders of magnitude with coherent x-rays. *Applied Sciences* **11** (2021).

45. H. Guo, S. Ramakrishnan, J. L. Harden, R. L. Leheny, Gel formation and aging in weakly attractive nanocolloid suspensions at intermediate concentrations. *J. Chem. Phys.* **135**, 154903 (2011).

46. A. H. Krall, D. A. Weitz, Internal dynamics and elasticity of fractal colloidal gels. *Phys. Rev. Lett.* **80**, 778–781 (1998).

47. A. Fluerasu, A. Moussaïd, A. Madsen, A. Schofield, Slow dynamics and aging in colloidal gels studied by x-ray photon correlation spectroscopy. *Phys. Rev. E* **76**, 010401 (2007).

48. J. H. Cho, R. Cerbino, I. Bischofberger, Emergence of multiscale dynamics in colloidal gels. *Phys. Rev. Lett.* **124**, 088005 (2020).

49. J.-P. Bouchaud, E. Pitard, Anomalous dynamical light scattering in soft glassy gels. *Eur. Phys. J. E* **6**, 231–236 (2001).

50. R. Bandyopadhyay, D. Liang, H. Yardimci, D. A. Sessoms, M. A. Borthwick, S. G. Mochrie, J. Harden, R. L. Leheny, Evolution of particle-scale dynamics in an aging clay suspension. *Phys. Rev. Lett.* **93**, 228302 (2004).

51. C. O. Osuji, C. Kim, D. A. Weitz, Shear thickening and scaling of the elastic modulus in a fractal colloidal system with attractive interactions. *Phys. Rev. E* **77**, 060402 (2008).

52. F. Augusto de Melo Marques, R. Angelini, E. Zaccarelli, B. Farago, B. Ruta, G. Ruocco, B. Ruzicka, Structural and microscopic relaxations in a colloidal glass. *Soft Matter* **11**, 466-471 (2015).

53. R. Poling-Skutvik, R. C. Roberts, A. H. Slim, S. Narayanan, R. Krishnamoorti, J. C. Palmer, J. C. Conrad, Structure dominates localization of tracers within aging nanoparticle glasses. *J. Phys. Chem. Lett.* **10**, 1784–1789 (2019).

54. F. Lehmkhler, F. Dallari, A. Jain, M. Sikorski, J. Mller, L. Frenzel, I. Lokteva, G. Mills, M. Walther, H. Sinn, F. Schulz, M. Dartsch, V. Markmann, R. Bean, Y. Kim, P. Vagovic, A. Madsen, A. P. Mancuso, G. Grbel, Emergence of anomalous dynamics in soft matter probed at the european xfel. *Proc. Natl. Acad. Sci. U. S .A.* **117**, 24110-24116 (2020).

55. A. Jain, F. Schulz, F. Dallari, V. Markmann, F. Westermeier, Y. Zhang, G. Grbel, F. Lehmkhler, Three-step colloidal gelation revealed by time-resolved x-ray photon correlation spectroscopy. *J. Chem. Phys.* **157**, 184901 (2022).

56. J. Song, Q. Zhang, F. de Quesada, M. H. Rizvi, J. B. Tracy, J. Ilavsky, S. Narayanan, E. D. Gado, R. L. Leheny, N. Holten-Andersen, G. H. McKinley, Microscopic dynamics underlying the stress relaxation of arrested soft materials. *Proc. Natl. Acad. Sci. U. S .A.* **119**, e2201566119 (2022).

57. P. Chaudhuri, L. Berthier, Ultra-long-range dynamic correlations in a microscopic model for aging gels. *Phys. Rev. E* **95**, 060601 (2017).

58. S. Romer, F. Scheffold, P. Schurtenberger, Sol-gel transition of concentrated colloidal suspensions. *Phys. Rev. Lett.* **85**, 4980–4983 (2000).

59. H. Tsurusawa, M. Leocmach, J. Russo, H. Tanaka, Direct link between mechanical stability in gels and percolation of isostatic particles. *Sci. Adv.* **5**, eaav6090 (2019).

60. S. Zhang, L. Zhang, M. Bouzid, D. Z. Rocklin, E. Del Gado, X. Mao, Correlated rigidity percolation and colloidal gels. *Phys. Rev. Lett.* **123**, 058001 (2019).

61. A. Jeong, J. Portner, C. P. N. Tanner, J. C. Ondry, C. Zhou, Z. Mi, Y. A. Tazoui, B. Lee, V. R. K. Wall, N. S. Ginsberg, D. V. Talapin, Colloidal dispersions of sterically and electrostatically stabilized pbs quantum dots: Structure factors, second virial coefficients, and film-forming properties. *ACS Nano* **18**, 33864-33874 (2024). PMID: 39630577.

62. M. Heinen, P. Holmqvist, A. J. Banchio, G. Nägele, Pair structure of the hard-sphere yukawa fluid: An improved analytic method versus simulations, Rogers-Young scheme, and experiment. *J. Chem. Phys.* **134**, 044532 (2011).

63. C. K. Ofosu, J. Kang, T. M. Truskett, D. J. Milliron, Effective hard-sphere repulsions between oleate-capped colloidal metal oxide nanocrystals. *J. Phys. Chem. Lett.* **13**, 11323-11329 (2022).

64. C. K. Ofosu, T. A. Wilcoxson, T.-L. Lee, W. D. Brackett, J. Choi, T. M. Truskett, D. J. Milliron, Assessing depletion attractions between colloidal nanocrystals. *Sci. Adv.* **11**, eadv2216 (2025).

65. B. Derjaguin, L. Landau, Theory of the stability of strongly charged lyophobic sols and of the adhesion of strongly charged particles in solutions of electrolytes. *Progress in Surface Science* **43**, 30-59 (1993).

66. E. J. W. Verwey, J. T. G. Overbeek, *Theory of the Stability of Lyophobic Colloids* (Elsevier, 1948).

67. P. K. Jha, V. Kuzovkov, B. A. Grzybowski, M. Olvera De La Cruz, Dynamic self-assembly of photo-switchable nanoparticles. *Soft Matter* **8**, 227–234 (2012).

68. A. Furukawa, H. Tanaka, Key role of hydrodynamic interactions in colloidal gelation. *Phys. Rev. Lett.* **104**, 245702 (2010).

69. H. Tsurusawa, S. Arai, H. Tanaka, A unique route of colloidal phase separation yields stress-free gels. *Sci. Adv.* **6**, eabb8107 (2020).

70. D. Wang, R. J. Nap, I. Lagzi, B. Kowalczyk, S. Han, B. A. Grzybowski, I. Szleifer, How and why nanoparticle's curvature regulates the apparent p K_a of the coating ligands. *J. Am. Chem. Soc.* **133**, 2192–2197 (2011).

71. B. K. Troudt, J. W. Vue, P. Bhlmann, Comparison of the kinetics of aldehyde sensing by covalent bond formation with hydrazines and hydroxylamines. *Tetrahedron* **119**, 132852 (2022).

72. E. V. Anslyn, D. A. Dougherty, *Modern Physical Organic Chemistry* (University Science Books, Sausalito, CA, 2005), chap. 7.4.2 Kinetic Analyses for Simple Mechanisms, pp. 383–386, first edn.

73. X. J. Cao, H. Z. Cummins, J. F. Morris, Structural and rheological evolution of silica nanoparticle gels. *Soft Matter* **6**, 5425-5433 (2010).

74. A. S. Negi, C. G. Redmon, S. Ramakrishnan, C. O. Osuji, Viscoelasticity of a colloidal gel during dynamical arrest: Evolution through the critical gel and comparison with a soft colloidal glass. *J. Rheol* **58**, 1557-1579 (2014).

75. L. Morlet-Decarnin, T. Divoux, S. Manneville, Slow dynamics and timecomposition superposition in gels of cellulose nanocrystals. *J. Chem. Phys.* **156**, 214901 (2022).

76. M. Heinen, P. Holmqvist, A. J. Banchio, G. Nägele, Pair structure of the hard-sphere yukawa fluid: An improved analytic method versus simulations, rogers-young scheme, and experiment. *J. Chem. Phys.* **134**, 044532 (2011).

77. T. B. Martin, T. E. I. Gartner, R. L. Jones, C. R. Snyder, A. Jayaraman, pyPRISM: A computational tool for liquid-state theory calculations of macromolecular materials. *Macromolecules* **51**, 2906-2922 (2018).

78. J. A. Anderson, J. Glaser, S. C. Glotzer, HOOMD-blue: A python package for high-performance molecular dynamics and hard particle Monte Carlo simulations. *Comp. Mater. Sci.* **173**, 109363 (2020).

79. D. Heyes, J. Melrose, Brownian dynamics simulations of model hard-sphere suspensions. *J. Nonnewton. Fluid Mech.* **46**, 1-28 (1993).

80. V. Ramasubramani, B. D. Dice, E. S. Harper, M. P. Spellings, J. A. Anderson, S. C. Glotzer, freud: A software suite for high throughput analysis of particle simulation data. *Comput. Phys. Commun.* **254**, 107275 (2020).